

Streamwise Vortices and Velocity Streaks in a Locally Drag-Reduced Turbulent Boundary Layer

H. L. Bai^{1,2,3} · Y. Zhou¹ · W. G. Zhang² · R. A. Antonia⁴

Received: 24 April 2017 / Accepted: 29 October 2017 / Published online: 12 October 2017
© Springer Science+Business Media B.V. 2017

Abstract This work aims to understand the changes associated with the near-wall streaky structures in a turbulent boundary layer (TBL) where the local skin-friction drag is substantially reduced. The Reynolds number is $Re_\theta = 1000$ based on the momentum thickness or $Re_\tau = 440$ based on the friction velocity of the uncontrolled flow. The TBL is perturbed via a local surface oscillation produced by an array of spanwise-aligned piezo-ceramic (PZT) actuators and measurements are made in two orthogonal planes using particle image velocimetry (PIV). Data analyses are conducted using the vortex detection, streaky structure identification, spatial correlation and proper orthogonal decomposition (POD) techniques. It is found that the streaky structures are greatly modified in the near-wall region. Firstly, the near-wall streamwise vortices are increased in number and swirling strength but decreased in size, and are associated with greatly altered velocity correlations. Secondly, the velocity streaks grow in number and strength but contract in width and spacing, exhibiting a regular spatial arrangement. Other aspects of the streaky structures are also characterized; they include the spanwise gradient of the longitudinal fluctuating velocity and both streamwise and spanwise integral length scales. The POD analysis indicates that the turbulent kinetic energy of the streaky structures is reduced. When possible, our results are compared with

✉ Y. Zhou
yuzhou@hit.edu.cn

H. L. Bai
hongleibai@ust.hk

¹ Institute for Turbulence-Noise-Vibration Interaction and Control, Shenzhen Graduate School, Harbin Institute of Technology, Shenzhen 518055, China

² State Key Laboratory of Aerodynamics, Mianyang 621000, China

³ Department of Civil and Environmental Engineering, Hong Kong University of Science and Technology, Clear Water Bay, Kowloon, Hong Kong SAR, China

⁴ School of Engineering, University of Newcastle, Callaghan, NSW 2308, Australia

those obtained by other control techniques such as a spanwise-wall oscillation, a spanwise oscillatory Lorentz force and a transverse traveling wave.

Keywords Turbulent boundary layer control · Streamwise vortices · Velocity streaks

Nomenclature

Latin symbols

A_o	Peak-to-peak oscillation amplitude at the actuator tip
A_{ω_x}	Size of streamwise vortex
D_{yz}	Velocity gradient tensor
f_o	Oscillation frequency
H_c	Height of vortex center
H_{12}	$= \delta^*/\theta$, Shape factor, where δ^* and θ are displacement and momentum thicknesses, respectively
L_c	Transverse spacing of adjacent vortex centers
N_c	Number of vortex center
Re_θ	$= U_\infty\theta/\nu$, Reynolds number based on momentum thickness
Re_τ	$= u_\tau\delta/\nu$, Reynolds number based on friction velocity
S	Spacing of adjacent streaks
U, U_∞	Local mean and free-stream streamwise velocities, respectively
u	Streamwise fluctuating velocity
u_τ	$= \sqrt{\bar{\tau}_w/\rho}$, friction velocity
W	Streak width
W_p	Perturbed spanwise velocity
w	Spanwise fluctuating velocity
x	Streamwise direction
y	Wall-normal direction
z	Spanwise direction

Greek symbols

δ_{99}	Boundary layer thickness defined by the location where $U = 99\%U_\infty$
θ	Momentum thickness
Λ_{ci}	$= (\omega_x/ \omega_x)\lambda_{ci}$, signed swirling strength
λ_r	Real eigenvalue
λ_{ci}	Vortex strength as indicated by eigenvalue of the local velocity gradient tensor
λ_z	Wavelength
v	Wall-normal fluctuating velocity
ρ	Flow density
$\bar{\tau}_w$	Averaged wall shear stress
$\phi_{i,i+1}$	($i = 1, 2, \dots, 15$), phase shift between adjacent actuator
ω_x	Streamwise vorticity
ω_y	Wall-normal vorticity

Abbreviations

PIV	Particle image velocimetry
POD	Proper orthogonal decomposition
TBL	Turbulent boundary layer
TKE	Turbulent kinetic energy

Superscripts

- + Normalization by wall units
- Ensemble average

1 Introduction

Almost half a century has elapsed since the observation of organized or coherent streaky structures in the near-wall region of a turbulent boundary layer (TBL) by Kline et al. [1] using hydrogen-bubble flow visualization. Our understanding of near-wall coherent structures has greatly improved since then (e.g., [2–4]), although many aspects of this flow have yet to be explored (e.g., [5, 6]). It is now widely accepted that near-wall coherent structures (e.g. quasi-streamwise vortices, velocity streaks, sweep, ejection and burst events) are closely connected to turbulence production and a close association exists between the quasi-streamwise vortices (referred to as streamwise vortices hereinafter) and a large wall shear stress (e.g., [7, 8]).

Near-wall coherent structures have been investigated experimentally, theoretically and numerically, including their salient characteristics, evolutionary dynamics and regeneration mechanisms. Visually, the coherent structures exhibit low- and high-speed streaks in the near-wall region [1, 9], arranged alternately along the spanwise direction (with an averaged spacing of 100 wall units) and elongated longitudinally (with an average length of 1000 wall units) in the buffer layer. These velocity streaks, together with turbulent events, are directly linked to streamwise vortices (e.g. [3, 10–12]). Low-speed streaks are a result of the ejection process induced by streamwise vortices on their updraught side. An inflectional instability may occur in the lifted flows, resulting in bursts which are the major source of turbulence production in the near-wall region [1]. On the other hand, sweeps on the down-draught side of streamwise vortices induce a strong fluid motion toward the wall, generating high-speed streaks, which are largely responsible for a large skin-friction drag. The velocity streaks contain most of the turbulent kinetic energy, while the streamwise vortices organize both the energy dissipation and Reynolds stresses [4]. For example, about 80% of the Reynolds stresses in the near-wall region are due to ejections and sweeps associated with the streamwise vortices [13]. Furthermore, the existing streamwise vortices may spawn offspring vortices through direct induction (e.g., [14, 15]); on the other hand, the local instabilities in the quasi-steady base flow may lead to the generation of new vortices, without necessarily requiring the presence of parent vortices (e.g., [3, 16]). Both scenarios of the vortex generation are self-sustaining [5].

The manipulation of near-wall coherent structures has been actively pursued using techniques such as riblets, compliant surfaces, wall suction and/or blowing, spanwise wall oscillation, oscillatory Lorentz force, and transverse or streamwise traveling waves. Gad-el-Hak [17], Karniadakis and Choi [18], Kim [11, 19] and Quadrio [20] provide excellent reviews of previous investigations. A detailed survey on the current drag reduction research has been given in Bai et al. [21]. A major objective of such manipulations is to reduce the skin-friction drag. The near-wall coherent structures are in general greatly modified when the drag reduction is substantial. Careful analysis of such modification often provides explanations for and/or some physical insight into underlying drag-reduction mechanisms. Using a spanwise oscillatory Lorentz force, Berger et al. [22] achieved a large drag reduction of 40% for an optimum oscillation period T^+ ($\equiv T/(\nu/u_\tau^2)$, where ν and u_τ are the kinematic viscosity of fluid and friction velocity, respectively) of 100 and observed an almost

complete suppression of near-wall streamwise vortices. Unless otherwise stated, superscript + denotes normalization by the wall units of the natural or uncontrolled TBL. The oscillating Lorentz force imposes a shear on the near-wall vortices such that those of the same sign as the applied shear survive, while those of opposite sign are suppressed. When the shear changes in the next phase, the remaining vortices are suppressed as well. A transverse wave traveling along the streamwise direction induced by Lorentz force may reduce the skin friction by up to 42% and suppress substantially the near-wall streamwise vortices, as a result of weakened coherent structures by wave-induced flow [23]. Using a streamwise traveling wave generated by wall deformation, Nakanishi et al. [24] observed that the turbulent organized structures were completely suppressed in a turbulent channel flow. Tomiyama & Fukagata [25] also noted substantially weakened streamwise vortices due to a spanwise traveling wave generated by wall deformation, which resulted in a maximum drag reduction of 13.4%. The effects on the drag reduction of Reynolds numbers and the parameters defining the wall-deformation-formed transverse traveling waves were investigated both numerically and experimentally by Koh et al. [26, 27] and Meysonnat et al. [28]. A maximum drag reduction of 11.4% was achieved. Compared with the uncontrolled near-wall flows, the velocity gradient and turbulent production were reduced at the troughs of the wave, together with increased heights for the maxima of turbulence intensity and wall-normal vorticity. Using a wave-like wall-normal body force deployed in the near-wall region of a turbulent channel flow, Mamori and Fukagata [29] achieved a 40% reduction in drag and observed a great attenuation of streamwise vortices. Based on selective wall deformation, Kang and Choi [30] observed weakened streamwise vortices when a drag reduction of 13–17% was obtained in a turbulent channel flow.

Another feature is the stabilized velocity streaks in the near-wall region provided the skin friction is substantially reduced, as observed over the spanwise oscillating wall by Choi et al. [31], Dhanak and Si [32] and Iuso et al. [33], and over the wall surface with the spanwise traveling wave by Du and Karniadakis [34], Du et al. [35] and Tomiyama and Fukagata [25]. The observations in the formers are linked to the regularization of streamwise vorticity [32], that is, the periodically generated vorticity promotes the decay of the natural streamwise vortices and thus weakens the velocity streaks. Du and Karniadakis [34] and Du et al. [35] deployed a spatial-force-generated transverse traveling wave and achieved a drag reduction in excess of 50%, associated with wide and stabilized ‘ribbons’ of low-speed streaks. They observed a regularized streamwise-vorticity layer, which was arranged alternately along the spanwise direction, with the near-wall streak pairs substantially weakened and even eliminated. This vorticity layer plays a role in suppressing the near-wall streak pairs and stabilizing the low-speed streaks. Tomiyama and Fukagata [25] observed stabilized low- and high-speed streaks, which were alternately and longitudinally displaced over the crests and troughs of the transverse traveling wave. Recently, using an array of spanwise-aligned discrete piezo-ceramic actuators to generate a transverse traveling wave, Bai et al. [21] achieved a local drag reduction of up to 50%, which is again associated with the stabilized longitudinal structures.

In spite of all the observations on the association of the stabilized streaks with large drag reduction, to date little attention has been given to these stabilized streaks. What is their origin? What are their important features? How do they compare with the natural streaks, not only qualitatively but also quantitatively? These issues are rather fascinating and of fundamental interest. Following the work of Bai et al. [21], we conduct here a close examination of these stabilized streaky structures. Use is made of statistical analysis, vortex detection, streaky structure identification, and proper orthogonal decomposition (POD) techniques

with a view to improving our understanding of the flow physics underlying the large drag reduction. The paper is organized as follows. The details of the experiment are described in Section 2, while the methods used for detecting the near-wall coherent structures are discussed in Section 3. The results are presented and discussed through Sections 4 to 6. This work is concluded in Section 7.

2 Experimental Details

Experiments were conducted in a closed-circuit wind tunnel, which has a 2.4 m-long test section of 0.6 m × 0.6 m. A flat plate, built with an elliptically-rounded leading edge, was tripped near the leading edge and placed horizontally in the test section to generate a fully developed TBL. Zero pressure gradient was ensured in the test section. One array of ceramic actuators was placed at 1.5 m downstream of the leading edge, where the corresponding Reynolds number is $Re_\theta = 1000$ based on momentum thickness $\theta (= 6.5 \text{ mm})$ or $Re_\tau = 440$ based on friction velocity $u_\tau (= 0.111 \text{ m/s})$ of the uncontrolled flow. Other important parameters of the natural TBL are boundary-layer thickness $\delta_{99} = 60 \text{ mm}$, shape factor $H_{12} = 1.4$, and free-stream velocity $U_\infty = 2.4 \text{ m/s}$ with a 0.7% turbulence intensity in the presence of the flat plate.

Figure 1a presents the layout of 16 PZT actuators flush-mounted with the wall and aligned along the spanwise direction (z). Each actuator, having a size of 22 mm × 2 mm × 0.33 mm (or $153 \times 14 \times 2.3$ wall units, length × width × thickness), was cantilever-supported, with the free end or active part (20 mm or 139 wall units long) pointing at the streamwise direction (x). There is a cavity underneath the active part of each actuator, which allows the actuator to oscillate up and down in the wall-normal direction (y) when driven by a sinusoidal voltage signal; see the cross-section of xy -plane in Fig. 1a. A laser vibrometer (Polytech OFV 3001 502) was used to measure the wall-normal motion or displacement of each PZT actuator in terms of peak-to-peak oscillation amplitude (A_o) at the actuator tip.

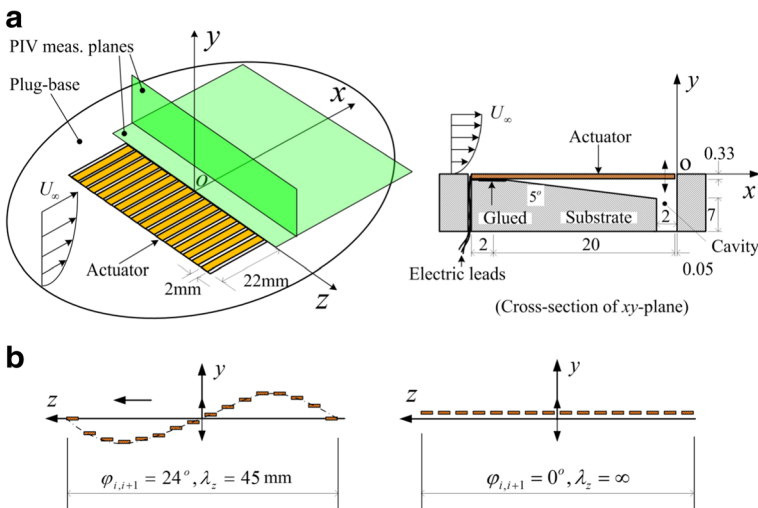


Fig. 1 **a** Layout of the spanwise aligned PZT actuators and PIV measurement planes; **b** transverse waves formed at $\phi_{i,i+1} = 24^\circ$ ($\lambda_z = 45 \text{ mm}$) and 0° (∞) by the actuators. This figure is adapted from Bai et al. [21]

The spacing between adjacent actuators is 1 mm (or 7 wall units), yielding a span of 45 mm (or 312 wall units) for the entire actuator array. With a specified phase shift $\phi_{i,i+1}$ ($i = 1, 2, \dots, 15$) between adjacent actuators, the 16 discrete actuators can form a transverse traveling wave along the spanwise direction (Fig. 1b). For example, at $\phi_{i,i+1} = 24^\circ$, a complete sinusoidal wave with a wavelength $\lambda_z = 45$ mm (or 312 wall units) can be formed by the 16 actuators; at $\phi_{i,i+1} = 0^\circ$, all the actuators oscillate up and down in phase, mimicking a flapping motion (with $\lambda_z = \infty$). The origin of the coordinate system is defined at the actuator tip, as shown in Fig. 1a; the fluctuating velocities along the x , y and z directions are designated as u , v and w , respectively. The dynamic characteristics of the actuator and its performance in disturbing the near-wall flow have been documented in detail in Bai et al. [21]. In the present work, the actuator array is working at the optimum control parameters, in terms of friction-drag reduction, that is, the oscillation frequency of the actuators is $f_o^+ = 0.65$, oscillation amplitude at the actuator tip is $A_o^+ = 2.22$, and wavelength of the generated transverse wave is $\lambda_z^+ = 416$ (or $\phi_{i,i+1} = 18^\circ$). These parameters are $f_o = 530$ Hz, $A_o = 0.3$ mm and $\lambda_z = 56$ mm in physical units. It has been observed that the large reduction in the local skin-friction force (around 30%) can be achieved at $f_o^+ \geq 0.39$, $1.75 \leq A_o^+ \leq 2.25$ and $\lambda_z^+ > 250$ [21]. The optimum control parameters (i.e., $f_o^+ = 0.65$, $A_o^+ = 2.22$ and $\lambda_z^+ = 416$) used in the present study are within the reported ranges.

Local skin-friction drag or wall shear stress $\bar{\tau}_w$ was estimated based on the streamwise mean velocity (\bar{U}) profile measured using a hotwire in the viscous sublayer of the boundary layer, as shown in Fig. 2. The local skin-friction reduction is defined by $\delta\tau_w = \frac{(\bar{\tau}_w)_{on} - (\bar{\tau}_w)_{off}}{(\bar{\tau}_w)_{off}} \times 100\%$, where subscripts *on* and *off* denote measurements with and without control, respectively. Figure 2a illustrates typical \bar{U} distributions measured at $x^+ = 35$ and

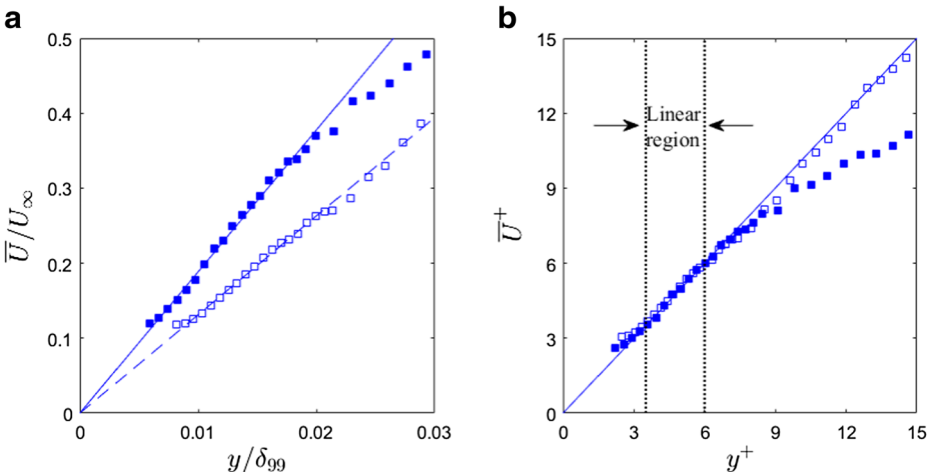


Fig. 2 Distributions of the mean streamwise velocity \bar{U}/U_∞ (a) and \bar{U}^+ (b) in the near-wall region, measured with a hot wire at $x^+ = 35$ and $z^+ = 0$: ■, without control; □, with control [$A_o^+ = 2.22$, $f_o^+ = 0.65$, and $\lambda_z^+ = 416$ (or $\phi_{i,i+1} = 18^\circ$), $\delta\tau_w = -30\%$]. The solid lines in (a) are based on least-squares-fitting of the data points at $y/\delta_{99} = 0.006 \sim 0.016$ for the uncontrolled flow and at $y/\delta_{99} = 0.01 \sim 0.02$ for controlled flow. Normalization in (b) is based on the actual wall units

$z^+ = 0$ downstream of the actuators. The data, with or without control, collapses well with the fitting lines over the range of $y/\delta_{99} = 0.006 \sim 0.02$. Once normalized by actual wall variables, the law of wall, i.e., $\overline{U}^+ = y^+$, is evident for both uncontrolled and controlled cases (Fig. 2b) over $y^+ = 3.5 \sim 6$, thus providing a validation for the $\overline{\tau}_w$ estimate. For $y^+ < 3$, \overline{U}^+ increases with decreasing y^+ due to heat transfer from the hot wire to the wall (e.g., [36]). With five repeated measurements, the standard deviation in the estimated wall shear stress is within $\pm 2\%$.

A Dantec PIV2100 system was deployed to measure near-wall streaky structures in the wall-parallel xz -plane at $y^+ = 5.5$, within the viscous sublayer, and in the cross-flow yz -plane at $x^+ = 35$ (Fig. 1a). The flow was seeded with smoke particles of about $1 \mu\text{m}$ in diameter generated from paraffin oil by a smoke generator. The Stokes number of the particle used is about 0.009, which is significantly smaller than 1. Two New wave standard pulse laser sources (wavelength = 532 nm, pulse duration = 10 ns, energy output ≤ 120 mJ/pulse and repetition rate ≤ 15 Hz) were used to generate a light sheet to illuminate the flow field. Particle images were captured using one CCD camera (double frames, 2048 pixels \times 2048 pixels). A Dantec FlowMap Processor (PIV2001 type) was used to synchronize image taking and flow illumination. The image magnification factor is 0.021–0.022 mm/pixel and the interval between two successive pulses is 80–100 μs , depending on the measurement plane. The middle 12 actuators were operated during PIV measurements. The area covered was $x^+ = 0\text{--}306$ and $z^+ = \pm 153$ in the xz -plane and $y^+ = 0\text{--}313$ and $z^+ = \pm 156.5$ in the yz -plane. The thickness of the laser light sheet was increased from 0.8 mm to 1.5 mm in the yz -plane measurement in order to capture more valid particles in the PIV images [37]. Spatial cross-correlation, with an interrogation window of 64 pixels \times 64 pixels and a 50% overlap, was employed to calculate velocity vectors, a total of 3969 (63 \times 63). The same number of vorticity data was obtained. Over 2000 pairs of images were taken in each plane, ensuring that the mean velocity and vorticity, and Reynolds stresses all statistically converge to $\leq 1\%$ uncertainty. Experimental uncertainties are quantified and given in Table 1 for the measured quantities such as mean velocities, vorticities, Reynolds stresses based on the PIV uncertainty propagation estimation [38]. The mean streamwise velocity has an uncertainty of 1% or less, the Reynolds stresses have uncertainties ranging from 2.9% to 12.3%, and the vorticities have uncertainties of 4.4–13.4%. Uncertainties for instantaneous velocities are presently estimated to be around 3% [37, 39]. It is worth pointing out that quantifying the uncertainties for the instantaneous velocities may involve all experimental and processing parameters – calibration, timing, imaging, seeding density, out-of-plane motion of particles, interrogation window size, etc. and remains to be a challenge (e.g., [40]). The Kolmogorov length scale is estimated to be in the range of 2.2–3.2 wall units for the region of the present concern, which is in the same order of magnitude as the spatial resolution (4.97) of the present PIV measurement.

Laser-illuminated smoke-wire flow visualization was conducted in the xz -plane to complement the PIV measurements. A nickel-chromium wire (diameter = 0.1 mm) was placed at $y^+ = 8$, parallel to the wall and normal to the streamwise flow direction. A continuous laser sheet (thickness = 0.8 mm) generated from an argon ion laser source of 4 W in power was used to illuminate the xz -plane at $y^+ = 10$. The flow field was recorded via a digital video camera at a rate of 25 frames per second. U_∞ was reduced to 1.5 m/s for improved flow visualization results, which should not affect the main conclusions given the present low Reynolds number [31].

Table 1 Experimental uncertainties (σ , standard deviation; ε , uncertainty; $\varepsilon\%$, uncertainty in percentage of the mean value)

U	\bar{U}	V	\bar{V}	W	\bar{W}	\overline{uu}	\overline{vv}	\overline{ww}	\overline{uv}	\overline{uw}	\overline{vw}	ω_x	$\omega_y \approx \partial u / \partial z$	L_c	H_c	$\overline{\Lambda_{ci}}(>0)$	$\overline{\Lambda_{ci}}(<0)$	$\overline{A_{ox}}(>0)$	$\overline{A_{ox}}(<0)$
σ^+	2.4	-	0.4	-	0.9	-	-	-	-	-	-	0.03	0.1	15.8	22.3	-	-	-	-
ε^+	-	0.05	-	0.03	-	0.02	0.18	0.03	0.02	0.05	0.01	0.002	0.03	2.48	2.48	0.002	0.002	10	10.8
$\varepsilon\%$	3%	0.7%	3%	-	3%	-	3.3%	9.9%	2.9%	-	12.3%	4.4%	13.4%	4%	6.8%	5.9%	5.9%	4.4%	4.8%

3 Detection of the Near-Wall Coherent Structures

The λ_{ci} -criterion [15, 41] is used to identify the near-wall streamwise vortices. In a three-dimensional (3D) turbulent flow, the local velocity gradient tensor has one real eigenvalue (λ_r) and one pair of complex conjugate eigenvalues ($\lambda_{cr} \pm i\lambda_{ci}$) provided that its characteristic equation has a positive discriminant. Physically, this means that the fluid particle exhibits a swirling and spiraling motion about the eigenvector corresponding to λ_r [41]. Furthermore, λ_{ci}^{-1} represents the orbit period of the fluid particle around the λ_r -vector. The condition $\lambda_{ci} = 0$ corresponds to an infinite orbit period and an infinitely long ellipse orbit, that is, the flow is a pure shear flow and $\lambda_{ci} > 0$ indicates a shorter and more circular ellipse or a vortex. The swirling strength of the vortex can be quantified by the λ_{ci} value [15]. Based on the present PIV-measured (v, w) in the yz -plane, the 2D form of the local velocity gradient tensor is given by $D_{yz} = \begin{bmatrix} \partial v / \partial y & \partial v / \partial z \\ \partial w / \partial y & \partial w / \partial z \end{bmatrix}$, which is associated with two real eigenvalues or one pair of complex conjugate eigenvalues ($\lambda_{cr} \pm i\lambda_{ci}$). The streamwise vortices in the yz -plane are then detected by the regions where $\lambda_{ci} > 0$. Further, a signed swirling strength Λ_{ci} defined by $\Lambda_{ci} = (\omega_x / |\omega_x|) \lambda_{ci}$, where ω_x is the streamwise vorticity, is used to denote the rotation direction of the detected vortices such that $\Lambda_{ci} > 0$ corresponds to the positive or clockwise vortices and $\Lambda_{ci} < 0$ to the negative or counter clockwise vortices.

Figure 3 shows one snapshot of the velocity vectors (v^+, w^+) and the detected vortices in the yz -plane at $x^+ = 35$. The solid white contours correspond to $\Lambda_{ci} = 0$ and denote the borders of the vortices. Individual positive ($\Lambda_{ci} > 0$) or negative ($\Lambda_{ci} < 0$) vortices can be clearly identified based on the iso-contours of Λ_{ci} -distribution as well as the velocity vectors. The shapes of vortices are irregular, i.e., not necessarily circular, as indicated by the enclosure of the white contours. For the sake of simplicity, the area enclosed by the white contour of $\Lambda_{ci} = 0$ is considered as the size of vortex (A_{ω_x}). The vortex center, as indicated by the white dot, is determined by the location where the maximum $|\Lambda_{ci}|$ is identified within the enclosure of the white contour. In case the maximum $|\Lambda_{ci}|$ happens to be at the border of the concerned zone, (e.g., $y^+ = 70$ and $z^+ = \pm 153$), this detection is considered to be invalid. The transverse distance (L_c) between two adjacent vortex centers and the distance (H_c) from the wall to the vortex center can then be determined. The uncertainty in estimating L_c and H_c is ± 2.48 wall units since the spatial resolution of the PIV measurement is $\Delta y^+ = \Delta z^+ = 4.97$ in the yz -plane.

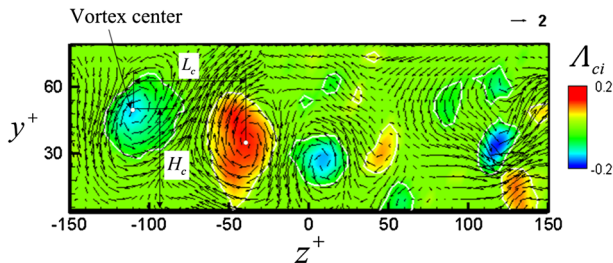


Fig. 3 Instantaneous velocity vectors (v^+, w^+) and streamwise vortices detected by the signed swirling strength $\Lambda_{ci} = [(\omega_x / |\omega_x|) \lambda_{ci}]$ in the yz -plane at $x^+ = 35$. Solid white contours ($\Lambda_{ci} = 0$) denote the borders of the vortices. White dots denote the vortex centers. Flow is into the figure

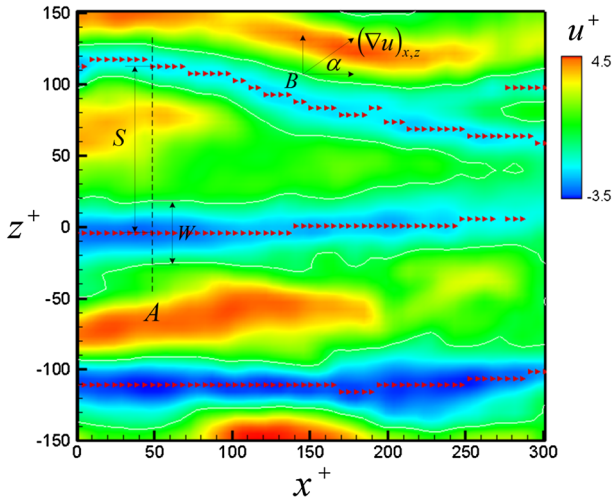


Fig. 4 Instantaneous velocity streaks detected from PIV-measured u^+ in the xz -plane at $y^+ = 5.5$. Solid white contours denote the borders of the low- and high-speed streaks. Right-pointing triangles denote the centers of the low-speed streaks. S and W are the spacing and width of the low-speed streaks, respectively, and $(\nabla u)_{x,z}$ is the velocity gradient of u across the streak border. α is the alignment angle of the velocity streak. Flow is left to right

Following Schoppa and Hussain [3], several characteristics of the velocity streaks are identified, e.g. the location of the center as well as the width, spacing and strength, from the PIV-measured (u, w) in the xz -plane at $y^+ = 5.5$. The length of the streaks, of the order of 1000 wall units, cannot be determined due to the limited PIV measurement area (306 wall units \times 306 wall units). One snapshot of the streaky structures is given in Figs. 4 and 5 to illustrate the detection process, as described below.

- (1) Contours of $u^+ < 0$ in Fig. 4 are identified with the low-speed streaks, and those of $u^+ > 0$ with high-speed streaks.

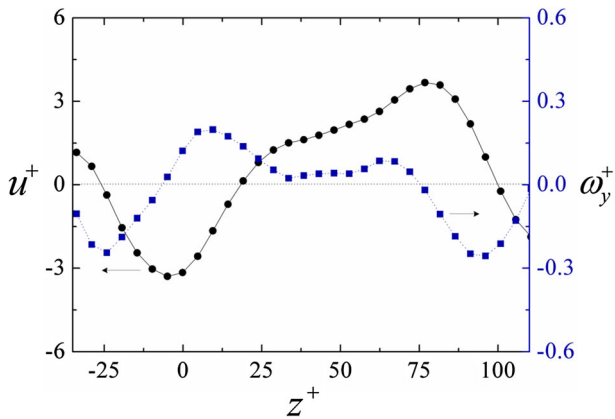


Fig. 5 Variations of u^+ and corresponding $\omega_y^+ \approx \partial u^+ / \partial z^+$ across the low- and high-speed streaks at location $A(x^+ = 50)$ in Fig. 4

- (2) The streak centers and edges can be determined from the variation of u^+ along the z direction. Take location A (Fig. 4) for example. We may find the variation of u^+ with z across the middle low- and high-speed streaks, as shown by the solid circles in Fig. 5. The streak center is identified with the minimum u^+ for the low-speed streak or the maximum u^+ for the high-speed streak and the streak edges with the zero-crossing points in z of u^+ , as inferred from a linear interpolation between the two points above and below $u^+ = 0$. In case of a streak splitting or two streaks merging, as illustrated by the upper two low-speed streaks at $x^+ > 250$ in Fig. 4, there will be two valleys of u^+ along the z direction. In this work, the identification of a streak strictly requires a zero-crossing at each edge, similarly to Iuso et al. [33]. As such, one streak center only is identified when the streaks are splitting or merging. See for example the right-pointing triangles denoting the low-speed streak centers in Fig. 4.
- (3) The spanwise gradient of u^+ , i.e. $\partial u^+ / \partial z^+ (\approx \omega_y^+)$, can be calculated, as shown by the solid squares in Fig. 5, and the local maximum $|\partial u^+ / \partial z^+|$ on either side of the streak center provides a measure for the streak strength. Evidently, $|\partial u^+ / \partial z^+|_{\max}$ may not necessarily take place at the streak edge (Fig. 5). At $z^+ > 0$, $|\partial u^+ / \partial z^+|_{\max}$ is inside the low-speed streak, not at the streak edge.
- (4) The other properties of the streak can be quantified, such as the width W of the streak, spacing S between adjacent streaks, and velocity gradient vector $(\nabla u)_{x,z} = \vec{i} \partial u / \partial x + \vec{k} \partial u / \partial z$ at the streak border (Fig. 3).

4 Control Effects on Streamwise and Spanwise Velocities, and Skin-Friction Drag

The distributions of mean streamwise velocity \bar{U}^+ and turbulent intensity u_{rms}^+ under the present optimum control parameters (i.e., $A_o^+ = 2.22$, $f_o^+ = 0.65$, and $\lambda_z^+ = 416$ (or $\phi_{i,i+1} = 18^\circ$)) are presented in Fig. 6. It can be seen that \bar{U}^+ and u_{rms}^+ are largely reduced in the near-wall region ($y^+ < 15$), which are associated with the significantly reduced skin-friction. Similar observations on the near-wall \bar{U}^+ - and u_{rms}^+ -distributions were made by

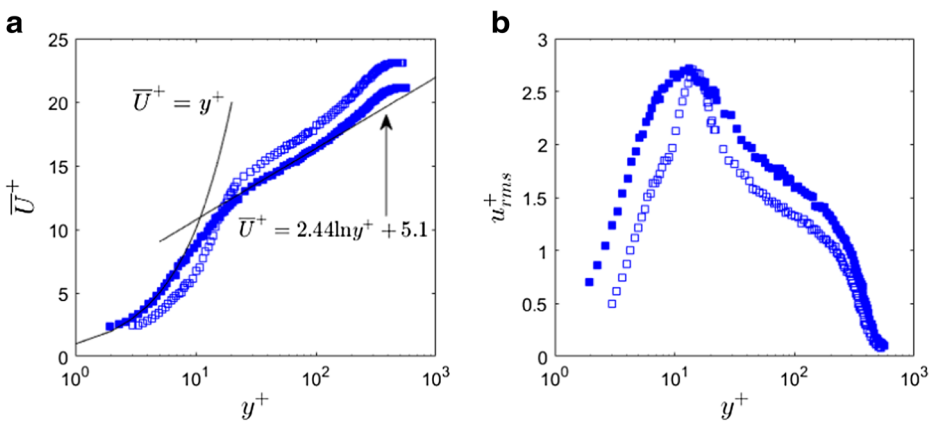


Fig. 6 Distributions of **a** mean streamwise velocity \bar{U}^+ and **b** turbulent intensity u_{rms}^+ : ■, without control; □, with control [$A_o^+ = 2.22$, $f_o^+ = 0.65$, and $\lambda_z^+ = 416$ (or $\phi_{i,i+1} = 18^\circ$), $\delta\tau_w = -30\%$]. $U_\infty = 2.4$ m/s

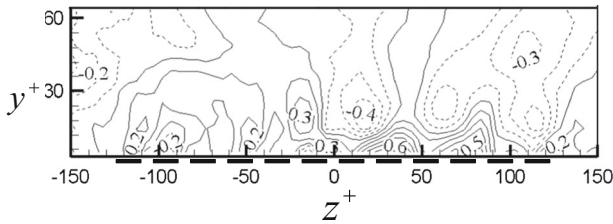


Fig. 7 Iso-contours of \overline{W}_p^+ , the time-averaged spanwise velocity under control in the yz -plane of $x^+ = 0$. The contour increment $\Delta = 0.1$. Solid and dotted lines denote positive and negative contour levels, respectively. Control parameters: $A_o^+ = 2.22$, $f_o^+ = 0.65$, and $\lambda_z^+ = 416$ (or $\phi_{i,i+1} = 18^\circ$). $U_\infty = 2.4$ m/s. The solid rectangles attached to the z^+ axis indicate actuators (12 elements are shown)

Du et al. [35] using a transverse traveling wave and Choi et al. [31] employing spanwise-wall oscillation. Beyond the buffer region at $y^+ > 20$, \overline{U}^+ is upwards shifted while u_{rms}^+ is reduced for the controlled flow. Figure 7 presents PIV-measured spanwise velocity in the yz -plane immediately downstream of the actuator tip at $x^+ = 0$. Discernibly, the actuator array generated a spanwise flow close to the wall. The spanwise velocity perturbation is mainly confined at $y^+ < 15$. Note that the spanwise velocity perturbation presently produced is weak, due to the discrete actuators of limited longitudinal extent. Furthermore, a careful examination of the smoke-wire flow visualization (see Fig. 16b) unveils the signature of the spanwise velocity perturbation; the smoke filaments were twisted to some extent immediately downstream of the actuator tips. Nevertheless, it should be pointed out that the present experimental control technique is not exactly the same as the numerical approach of a transverse traveling wave in Du et al. [35]. First, the actuators are discrete in nature and it is hence impossible to form a perfect wave, as Du et al. managed. Secondly, the wall-normal-motion-produced transverse wave is not identical to the Lorentz-force-induced one; the forcing of the near-wall flow structure originates from the wall-based oscillation for the former but from the spatial force for the latter.

Dependence of the local skin-friction reduction $\delta\tau_w$ on the streamwise (x^+) and spanwise (z^+) locations are presented in Fig. 8, which is replotted based on the data in Bai et al. [21]. It can be seen that $\delta\tau_w$ depends on the measurement location. As x^+ increases, $\delta\tau_w$ diminishes rapidly downstream for $x^+ < 52$, though slowing down for larger x^+ , and approaches zero at $x^+ \approx 160$. The spanwise change of $\delta\tau_w$ exhibits a tooth-like variation, which is not unexpected in view of the deployment of the discrete actuators. The $\delta\tau_w$ is in general larger between adjacent actuators than at the symmetry plane of each actuator. The spanwise-averaged value of the local skin-friction drag reduction is -23% at $x^+ = 35$ under the optimum control parameters.

5 Results for Streamwise Vortices

Similarly to Choi et al. [31] and Gouder and Morrison [42], Bai et al. [21] noted that the root mean square value of the hotwire-measured streamwise fluctuating velocity changed significantly in the region $y^+ = 0\text{--}20$ under control, as did the mean turbulent energy dissipation rate. On the other hand, little change was observed above $y^+ = 20$. The observations suggest that the control may have a limited effect on the streamwise vortices beyond $y^+ = 20$. As such, the present detections were made only in the region $y^+ = 0\text{--}20$. A total of

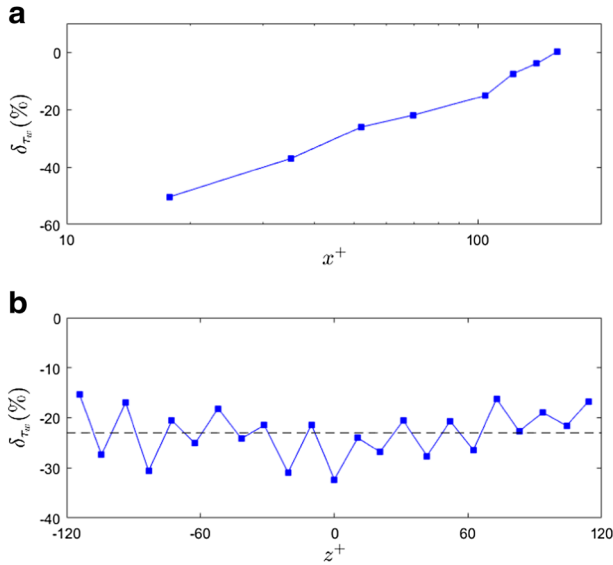


Fig. 8 Dependence of δ_{τ_w} on **a** x^+ at $z^+ = 0$ and **b** z^+ at $x^+ = 35$. The horizontal dashed line in panel **b** denotes the spanwise-averaged value of $\delta_{\tau_w} = -23\%$. The control parameters are $A_o^+ = 1.94$, $f_o^+ = 0.39$, and $\lambda_z^+ = 416$ (or $\phi_{i,i+1} = 18^\circ$), $U_\infty = 2.4$ m/s

7243 and 7876 streamwise vortices were detected in the yz -plane at $x^+ = 35$ with and without control, respectively. Figure 9 presents histograms of the swirling strength Λ_{ci} of the detected streamwise vortices. Unless otherwise stated, the histograms are normalized so that the sum is unity. Without control, the distribution of the Λ_{ci} values appears symmetrical about $\Lambda_{ci} = 0$, the highest values occurring at $|\Lambda_{ci}| = 0.015$. However, once the control is introduced, the distribution exhibits an asymmetry, the peak on the left exceeding that on the right, and we see an appreciable increase at large $|\Lambda_{ci}|$, particularly in the negative tail of $\Lambda_{ci} < -0.03$, indicating that the negative or counter clockwise vortices are strengthened. The number (N_c) and averaged swirling strength ($\bar{\Lambda}_{ci}$) of the negative vortices rise by 11.9% and 11.1%, respectively, which is considerably larger than the change (5.5% and 5.1%, respectively) for the positive vortices (Table 2). The observations are linked to the wall-based transverse traveling wave. When the wave travels along the positive z direction,

Fig. 9 Histograms of the signed swirling strength Λ_{ci} of streamwise vortices at $x^+ = 35$ and $y^+ = 0 \sim 20$: \blacksquare , uncontrolled; \square , controlled

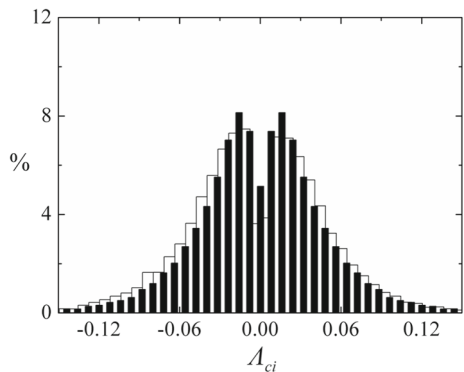


Table 2 Streamwise vortices in the yz -plane at $x^+ = 35$ ($y^+ \leq 20$) with and without control (N_c , vortex center number; $\bar{\Lambda}_{ci}$, averaged swirling strength; \bar{H}_c^+ , averaged vortex center height; \bar{L}_c^+ , averaged vortex center spacing; $\bar{A}_{\omega_x}^+$, averaged vortex size)

	Control	N_c	$\bar{\Lambda}_{ci}$	\bar{H}_c^+	\bar{L}_c^+	$\bar{A}_{\omega_x}^+$
Positive vortices	Off	3566	0.0375	12.1	62.8	227.1
	On	3762	0.0394	11.4	47.6	205.3
	(On-Off)/Off	5.5%	5.1%	− 5.6%	− 24.2%	− 9.6%
Negative vortices	Off	3677	− 0.0368	11.9	61.6	232.8
	On	4114	− 0.0409	10.9	48.3	204.3
	(On-Off)/Off	11.9%	11.1%	− 8.4 %	− 21.6%	− 12.2%

the negative vortices are mainly induced immediately above the wall in the near-wall region. Figure 10 presents an instantaneous snapshot of the iso-contours of Λ_{ci} in the presence of control, showing that a larger number of smaller vortices (most of them of similar size and rotation) occur rather regularly near the wall, as compared with the case without control (Fig. 6). Then, it seems plausible that the regularly arranged streamwise-vortex layer in the near-wall region mainly comprises the strengthened negative vortices.

Figure 11 displays histograms of H_c , L_c and A_{ω_x} of the detected streamwise vortices in the yz -plane at $x^+ = 35$ and $y^+ \leq 20$ with and without control. In the absence of control, the percentage of H_c (Fig. 11a & b) tends to drop gradually with increasing H_c^+ up to $H_c^+ \approx 50$, with a minor local peak occurring at $H_c^+ \approx 15$, which is consistent with the model of near-wall streamwise vortices proposed by Kim et al. [9], where the center of the vortex is at $y^+ \approx 20$. This small difference is not unexpected since $\Delta y^+ = 4.9$ in the present PIV measurement and in the range 0.05–4.4 in Kim et al.’s simulation. The histogram of L_c (Fig. 11c & d) has its maximum at $L_c^+ = 35$ (the average value L_c^+ is 62) and its tail extends to almost $L_c^+ = 240$. The percentage occurrence of $\bar{A}_{\omega_x}^+$ reduces monotonically with increasing $\bar{A}_{\omega_x}^+$, the averaged size $\bar{A}_{\omega_x}^+$ of the detected vortices in the region $y^+ \leq 20$ being about 230 (Table 2). Once control is applied, a number of significant changes can be observed. Firstly, the percentage occurrence of H_c (Fig. 11a & b) increases considerably for $H_c^+ < 20$, particularly for the negative vortices (Fig. 11a), while the average value H_c^+ is reduced by about 8.4%, beyond the experimental uncertainty (Table 2). This observation supports the occurrence of more negative vortices in the near-wall region when control is applied. Secondly, the percentage occurrence of L_c grows significantly at small L_c^+ (Fig. 11c & d), the averaged value of L_c being reduced by 24.2% and 21.6%, respectively. The observation

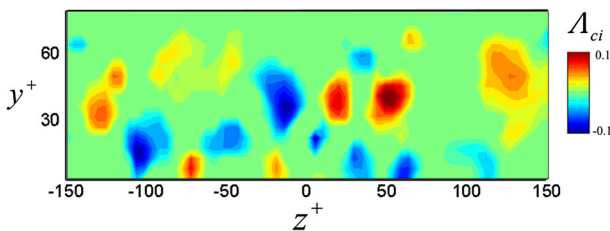


Fig. 10 Instantaneous streamwise vortices, as shown in the iso-contours of Λ_{ci} , in the yz -plane at $x^+ = 35$ in the presence of control. Flow is into the figure

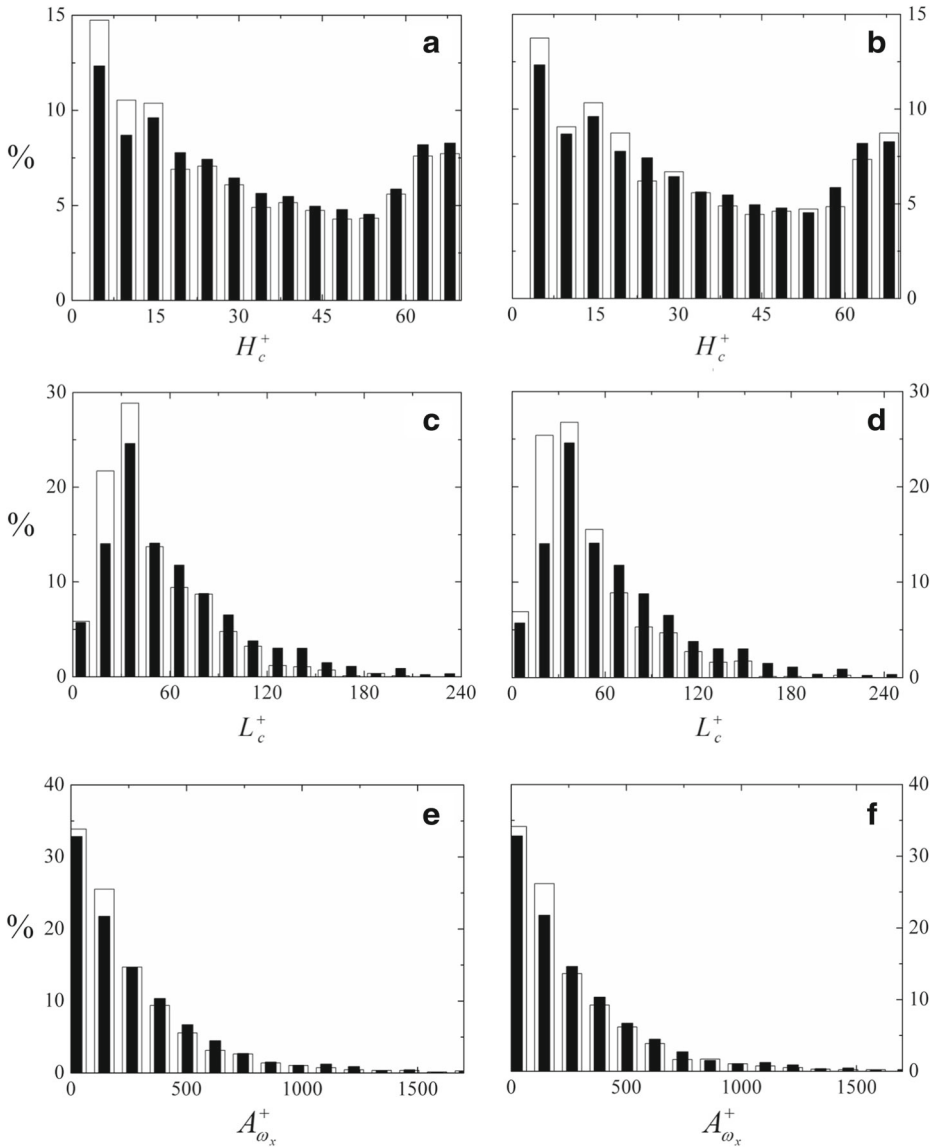


Fig. 11 Histograms of the height H_c^+ (a & b), spacing L_c^+ (c & d) and size $A_{\omega_x}^+$ (e & f) of the negative-signed (a, c & e) and positive-signed (b, d & f) vortices in the yz -plane at $x^+ = 35$: ■, uncontrolled; □, controlled

implies that the vortices are more closely spaced in the controlled flow, as is confirmed by the flow visualization to be shown later. Thirdly, the percentage of $\overline{A_{\omega_x}^+}$ appears to decrease at large values and increase at low values, the averaged values being reduced by 9.6% and 12.2% for positive and negative vortices, respectively. It is interesting to note that $\overline{A_{\omega_x}^+}$ is increased mostly at $A_{\omega_x}^+ = 130$ (Fig. 11e & f), i.e., the control generates additional vortices of similar size, which is again verified by the flow visualization data.

The significant change in the streamwise vortices suggests a variation in the structure of velocity correlations under control. Note that the Reynolds shear stress $\overline{u^+v^+}$ has not been measured in the present experiment. Figure 12 contains histograms for the correlations $\overline{u^+u^+}$, $\overline{w^+w^+}$ and $\overline{u^+w^+}$ in the xz -plane at $y^+ = 5.5$ ($x^+ \leq 160$) (Fig. 12a-c) and $\overline{v^+v^+}$, $\overline{w^+w^+}$ and $\overline{v^+w^+}$ in the yz -plane at $x^+ = 35$ ($y^+ \leq 20$) (Fig. 12d-f) with and without control. The histograms are calculated from a total of 2079 data points in the xz -plane and 252 points in the yz -plane. Without control (see closed histograms), the histograms of $\overline{u^+u^+}$, $\overline{w^+w^+}$ and $\overline{u^+w^+}$ in the xz -plane at $y^+ = 5.5$ (Fig. 12a-c) are approximately symmetrical about their means (i.e., $\overline{u^+u^+} = 5.5$, $\overline{w^+w^+} = 0.82$ and $\overline{u^+w^+} = 0$). The slight asymmetry can be mainly ascribed to the measurement difficulties in the region very close to the wall due for example to slight misalignments of the laser sheets to the wall surface or possibly contaminated illumination from wall reflections. The finite number of data (2000 pairs of PIV images) may also contribute to this slight asymmetry. For the uncontrolled flow in the yz -plane of $x^+ = 35$ ($y^+ < 20$), the marked rise in the histograms of $\overline{v^+v^+}$ over the range from 0.12 to 0.2 (Fig. 12d), is consistent with the slow increase of $\overline{v^+v^+}$ from $y^+ = 0$ to 15 (e.g., [9]). The histograms of $\overline{v^+w^+}$ (Fig. 12f) in the yz -plane of $x^+ = 35$ are obviously asymmetric, with a relatively long trail extended to $\overline{v^+w^+} \approx -0.26$, due to the inhomogeneous nature of the near-wall flow structures along the wall-normal y direction. Once the perturbation is introduced (see open histograms), several changes can be observed. Firstly, the histograms of $\overline{w^+w^+}$ in both xz - and yz - planes spread considerably. For the histograms of $\overline{w^+w^+}$ in the xz -plane (Fig. 12b), the distribution reaches up to $\overline{w^+w^+} = 1.25$ on the right-hand side; for the histograms of $\overline{w^+w^+}$ in the yz -plane (Fig. 12e), the spread on both sides is observed, with the distribution extended to $\overline{w^+w^+} = 0.81$ and 2.5 on the left- and right-hand sides, respectively. The observation suggests that strong spanwise fluctuating velocities are induced by the transverse traveling wave and the resultant streamwise vortices. Touber and Leschziner [43] observed an increased $\overline{w^+w^+}$, due to the periodic variation in w induced by the spanwise-wall oscillation. Secondly, the histograms

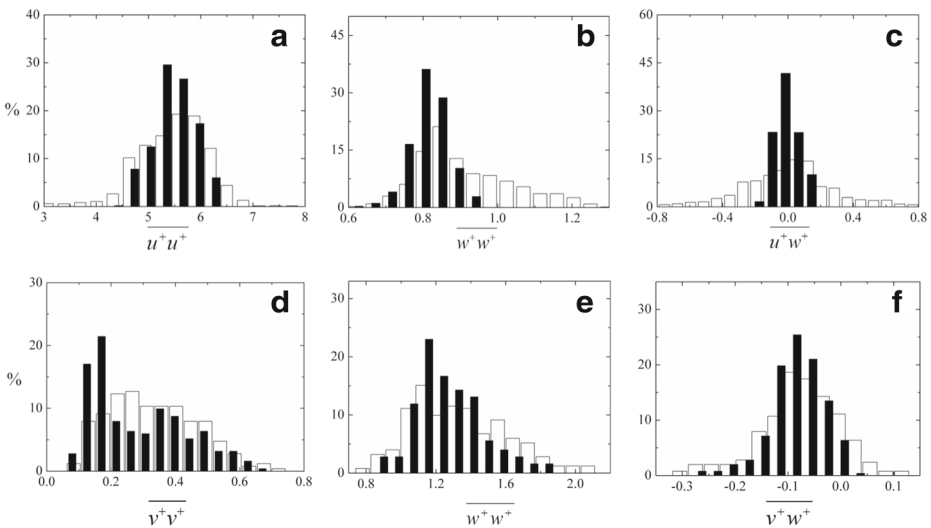


Fig. 12 Histograms of correlations $\overline{u^+u^+}$, $\overline{w^+w^+}$ and $\overline{u^+w^+}$ in the xz -plane at $y^+ = 5.5$ ($x^+ < 160$) and $\overline{v^+v^+}$, $\overline{w^+w^+}$ and $\overline{v^+w^+}$ in the yz -plane of $x^+ = 35$ ($y^+ < 20$): ■, uncontrolled; □, controlled

of $\overline{u^+w^+}$ exhibit much wider tails in the xz -plane (Fig. 12c), compared with the natural flow, with the distribution extended up to $u^+w^+ = \pm 0.8$ on both sides, indicating a strong shear induced by the strengthened streamwise vortices of smaller size (Figs. 9–11). The histogram of $\overline{v^+w^+}$ in the yz -plane (Fig. 12f) is also shifted appreciably toward larger magnitudes on both sides; the distribution extends to $\overline{v^+w^+} = 0.12$ on the right-hand side and -0.3 on the left-hand side. Thirdly, there is a considerable increase in the probability of $\overline{v^+v^+}$ (Fig. 12d) in the range 0.20–0.33 with control, which may be ascribed to the wall-normal oscillations of the actuators. Over the spanwise-oscillating wall, however, Touber and Leschziner [43] observed a drastic reduction in $\overline{v^+v^+}$, up to 80% in the viscous sublayer, which essentially depletes the wall-normal momentum exchange in the near-wall region and hence disrupts the turbulence contribution to the wall shear stress.

6 Results for Velocity Streaks

The variation in the velocity streaks may be quantified via the maximum velocity magnitude, u_{\max}^+ , of the streaks, the spanwise gradient of the fluctuating streamwise velocity, $\partial u / \partial z$, along the edges of the streaks, the strength and integral length scales of the streaks. Histograms of u_{\max}^+ for low- and high-speed streaks in the xz -plane of $y^+ = 5.5$ are shown in Fig. 13 with and without control. The value of u_{\max}^+ is estimated from the detected streak center across each z -cut in the plane of concern ($x^+ \leq 160$). The histogram of u_{\max}^+ is obtained from 162985 data points for the low-speed streaks (Fig. 13a) and 170781 for the high-speed streaks (Fig. 13b). Evidently, the $|u_{\max}^+|$ of the streaks under control is shifted toward the lower magnitude, particularly for the low-speed streaks, compared to that without control. With control, u_{\max}^+ occurs mostly at $|u_{\max}^+| = 2.74$ (Fig. 13a), about 8% smaller than without control; the averaged value is reduced by about 7.5%. These changes are clearly beyond the experimental uncertainty of 3% in U . The histogram of u_{\max}^+ for the controlled high-speed streaks is also shifted appreciably toward smaller magnitudes (Fig. 13b), with the averaged value reduced by about 4%. That is, the perturbation has a significant effect on the ejection motions associated with the low-speed streaks and also the sweep motions associated with the high-speed streaks, though to a smaller extent. This observation is internally consistent with the fact that the perturbation originates at the wall. Further, the presence of

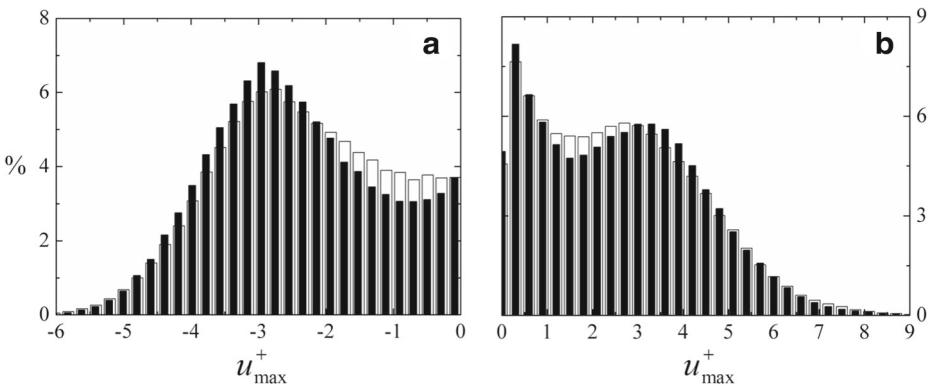
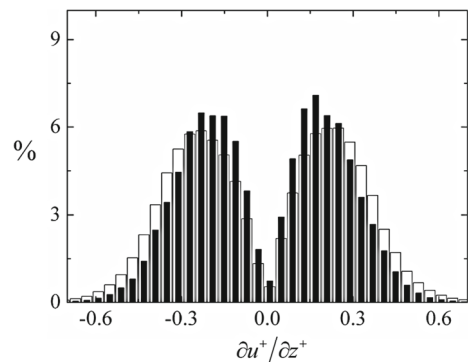


Fig. 13 Histograms of the maximum u^+ , u_{\max}^+ , of the low-speed (a) and high-speed streaks (b) in the xz -plane at $y^+ = 5.5$ ($x^+ < 160$): ■, uncontrolled; □, controlled

the externally generated streamwise vortices in the near-wall region, which are arranged in a pseudo-regular fashion, small in size but strong in swirling strength, may severely interfere with, if not interrupt, low-speed fluid ejections away from the wall as well as high-speed fluid sweeps toward the wall. A large decrease in u_{\max}^+ was also evidenced with other control techniques. With a spanwise-wall oscillation, for example, there is a reduction of about 30% in the ensemble-averaged $\langle u_{\max}^+ \rangle$, reflecting substantially suppressed bursting [44].

The velocity gradient $\partial u/\partial z$ of the streaks makes a predominant contribution to the wall-normal vorticity (ω_y), i.e., $\partial u/\partial z \approx \omega_y$, and presumably the stretching of the streaks [33]. Figure 14 presents the histograms of $\partial u^+/\partial z^+$ at the streak borders with and without control. Obviously, the histogram of $\partial u^+/\partial z^+$ is significantly modified by the control, with a shift to larger $|\partial u^+/\partial z^+|$. As shown in Figs. 9 & 10 and also according to the schematic model proposed by Bai et al. [21] (see their Fig. 22), smaller and more regularized streamwise vortices are generated by the discrete transverse traveling wave. In fact, the velocity streaks shrink in width and spacing but increase in number under control. Bai et al. [21] observed a decrease in width and spacing by 12.2% and 13.5%, respectively, for the low-speed streaks, but an increase in number by 14.6%. The present calculations, based on the detection of streaky structures (Section 3), indicate a decrease in width and spacing by 13.4% and 16.1%, respectively, but an increase in number by 18.2% for the high-speed streaks. The change in the histogram of $\partial u^+/\partial z^+$ (Fig. 14) suggests an increase in the streak strength because the maximum $|\partial u^+/\partial z^+|$ across the streaks is an indicator of the streak strength [3]. This is indeed confirmed by the histograms of $|\partial u^+/\partial z^+|_{\max}$ in Fig. 15, where the histogram under control is shifted toward the larger $|\partial u^+/\partial z^+|_{\max}$ for both the low- and high-speed streaks. The increased streak strength, 13.0% and 15.4% for low- and high-speed streaks, respectively, confirms the more intense stretching of the controlled velocity streaks. This seems consistent with the enhanced streamwise vortices, notwithstanding their reduced size (Fig. 11). The present observations differ from those by Iuso et al. [33] who used a spanwise-wall oscillation. They observed an opposite shift toward smaller $|\partial u^+/\partial z^+|_{\max}$ and a drop by 15% in the streak strength. This disparity is linked to the two approaches employed. The present discrete actuators produce a layer of regularized streamwise vortices in the near-wall region, resulting in more regular and smaller-scale longitudinal structures (Fig. 16), together with an increased number of velocity streaks of smaller width and spacing but with an increased spanwise velocity gradient. On the other hand, the connections between the low-speed streaks and the streamwise vortices were strongly interrupted by the spanwise oscillation of the entire wall (e.g., [45]) and,

Fig. 14 Histograms of $\partial u^+/\partial z^+$ at the streak borders in the xz -plane at $y^+ = 5.5$ ($x^+ < 160$): ■, uncontrolled; □, controlled



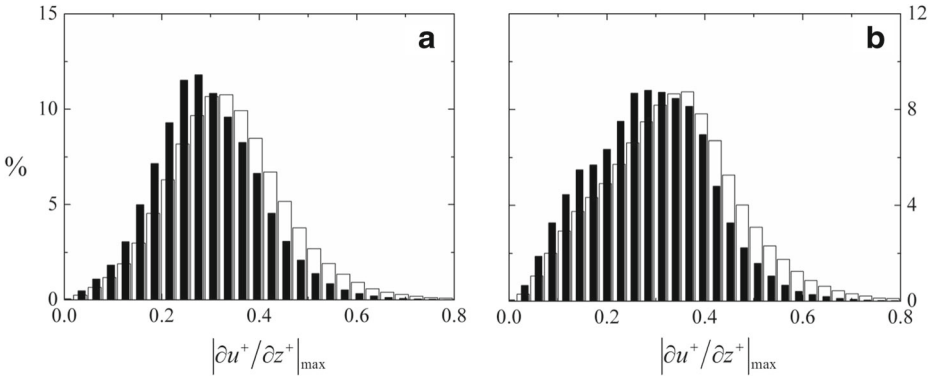


Fig. 15 Histograms of $|\partial u^+ / \partial z^+|_{\max}$ across the low-speed (a) and high-speed streaks (b) in the xz -plane at $y^+ = 5.5$ ($x^+ < 160$): ■, uncontrolled; □, controlled

consequently, the low-speed streaks coalesce, forming fewer and wider streaks of increased spacing but reduced spanwise velocity gradient [33].

There is a fundamental difference between the present control and that based on the spanwise wall motion. The former directly injects energy into the wall-normal velocity fluctuation. As a result, more near-wall streamwise vortices are formed, which are smaller in size and more intense (i.e., a larger eigenvalue λ_{ci} of the local gradient velocity tensor) and with a more regular spatial arrangement. For example, the number and strength of the negative streamwise vortices are increased by 11.9% and 11.1%, while their average size reduced by 12.2%, respectively. Meanwhile, the near-wall velocity streaks are characterized by smaller width and separation but larger strength, which is indicated by the maximum gradient, with respect to z , of u within the streak; the width and spacing of the low-speed streaks are reduced by 12.2% and 13.5%; their strength is increased by 13.0%. On the other hand, the spanwise wall oscillation suppresses indirectly wall-normal velocity fluctuations and further eliminates completely or substantially the near-wall streamwise vortices (e.g., [22]). The near-wall velocity streaks are also largely weakened and stabilized, with increased spacing [33]. Consequently, the near-wall bursting events, which are associated with the downwash of high-momentum fluid toward the wall, were suppressed, thus resulting in a significant reduction in skin-friction drag [18].

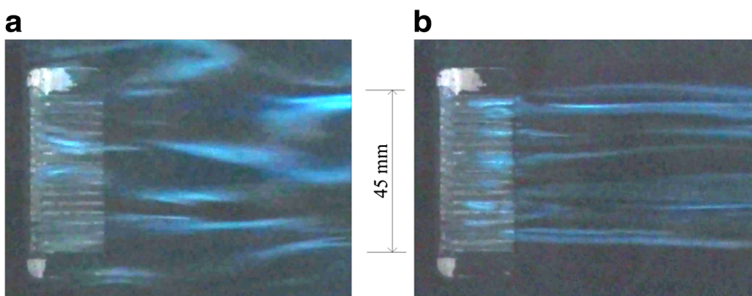


Fig. 16 Typical instantaneous flow structures in the xz -plane from a smoke-wire flow visualization: a uncontrolled, b controlled. The smoke wire was placed at $y^+ = 8$ and the laser sheet at $y^+ = 10$. Flow is left to right and $U_\infty = 1.5$ m/s

The difference between the two techniques may be viewed from another perspective. We have measured δ_{τ_w} beyond $x^+ \approx 160$ where the flow recovery to its natural state, there was no overshoot in δ_{τ_w} , that is, δ_{τ_w} remained to be zero (Fig. 8). Using different numbers of actuators, i.e., 8, 6, 4 and 2, Yang [46] investigated the effect of finite spanwise extent of the present actuators on the local skin-friction reduction and found that the number of actuators has a negligible effect on the drag reduction (i.e., the maximum drag reduction is essentially unchanged). The downstream recovery of skin-friction is slowed down with increasing the spanwise extent of the actuation array. Based on an actuation array of 2 actuators and different control schemes, Qiao et al. [47] also achieved a large drag reduction. Apparently, the natural flow around the control area is expected to be entrained into the perturbed region due to the highly three-dimensional near-wall flows such as meandering streaky structures. The increased spanwise width of the actuators acts to prolong this process. The control efficiency, in terms of the ratio between the power saved and consumed, is very low, in the same order as that when a spanwise oscillating Lorentz force [22] or wavy Lorentz force [23] was used. This is in distinct contrast to the wall oscillation technique that produces drag reduction over the entire oscillating wall. Note that the reduced skin-friction drag due to the spanwise-wall oscillation also recovers rapidly to its natural value at about $2\delta_{99}$ downstream of the trailing edge of the oscillating wall [48, 49].

The velocity streaks under the present control look opposite in appearance to those observed for the transverse traveling wave [25, 34, 35], the spanwise oscillatory Lorentz force (e.g., [22]), the riblets wall (e.g., [50]) and the spanwise oscillating wall (e.g., [31–33]). Under the present control, as shown in Fig. 16, the large-scale streaky structures are no longer observable; instead, more organized, stable and smaller-scale longitudinal structures appear. Naturally, the number of identified low- and high-speed streaks and vortices increases, which is associated with the diminished streak width and spacing as well as the reduced vortex size and spacing (Table 2). However, the spanwise gradient of velocities is larger (Fig. 14), accounting for a growth in the streak strength (Table 2; Fig. 9). On the other hand, the velocity streaks observed in the aforementioned studies display an increase in width and spanwise spacing. Nevertheless, an unmistakable common feature for all the aforementioned and present visualizations associated with significant drag reduction is that the streaky structures are more ordered than in the natural case. It would appear that this increased organization is a generic feature of the near-wall flow produced by a variety of drag reduction strategies. However, the mechanism underpinning the present drag reduction may differ from others. One wavy layer of highly regularized streamwise vortices has been produced by the wall-based oscillating actuators. This layer plays two distinct roles on the drag reduction. Firstly, it acts as a barrier that prevents the large-scale coherent structures from reaching the wall, thus interfering with the turbulence production cycle in the near-wall region. This is consistent with Tomiyama and Fukagata's [25] suggestion, based on the DNS data of turbulent channel flows over spanwise traveling wave-like wall deformation, that the spanwise flow induced by the pumping effect of the deformed wall plays a role of preventing large-scale quasi-streamwise vortices from the wall, thus suppressing these large-scale coherent structures and resulting in large skin-friction reduction. Secondly, this layer of streamwise vortices is highly dissipative, associated with a great increase in dissipation rate [21]. Qiao et al.'s [47] measurement of the dissipation in the boundary layer, whose skin friction drag was substantially reduced using the same technique, confirmed the second role. A rise in the predominant dissipation component by up to 5 times in the near-wall region was observed. The possibly reduced turbulence production and meanwhile the enhanced turbulence dissipation may lead to relaminarization, which is fully consistent with the observation from flow visualization (Fig. 16). Similar results have also been observed by

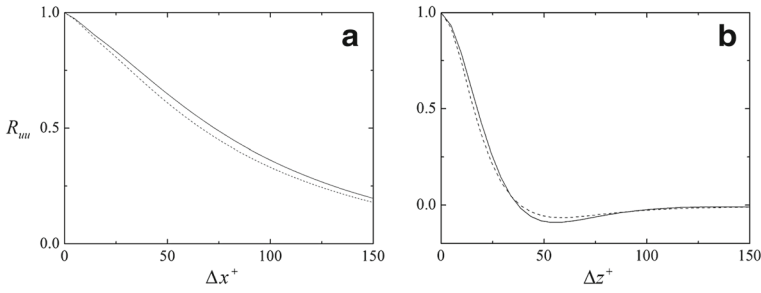


Fig. 17 Two-point correlation function R_{uu} of u in the xz -plane at $y^+ = 5.5$. **a** Streamwise slice at $\Delta z = 0$, **b** spanwise slice at $\Delta x = 0$: —, uncontrolled; ----, controlled

Antonia et al. [51]. Orderly and stabilized near-wall streaks were observable immediately downstream of a suction strip until their final disappearance, i.e., when the flow returned to a laminar state (see e.g. Fig. 10b in [51]). On the other hand, the mechanisms for previously reported other techniques could be quite different. Take the transverse oscillating wall technique [31–33] for example. The low-speed streaks coalesce under the spanwise-wall oscillation, forming fewer and wider low-speed streaks with increased spacing, thus resulting in large drag reduction.

The spatial correlation of the streamwise fluctuating velocities u in the xz -plane at $y^+ = 5.5$ may provide a measure of the streak length scales. The spatial correlation function of any two quantities A and B is defined as

$$R_{AB}(\Delta x, \Delta z) = \overline{A(x, z)B(x + \Delta x, z + \Delta z)} / (\sigma_A \sigma_B),$$

where σ_A and σ_B are the standard deviations of A and B , respectively, Δx and Δz are the separations between A and B , and the overbar denotes an ensemble average over all realizations. The correlation is normalized such that $R_{AB}(0, 0) = 1$. Figure 17 shows the variation in R_{uu} with Δx at $\Delta z = 0$ and with Δz at $\Delta x = 0$. Clearly, both longitudinal and lateral integral scales, as indicated by the areas under the curves, are reduced with

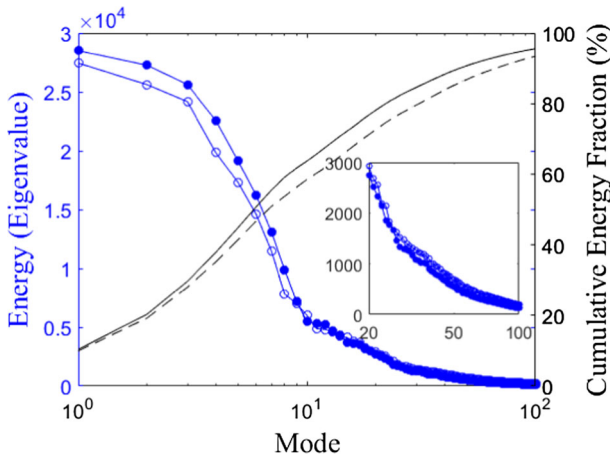


Fig. 18 Energy (eigenvalue) and cumulative energy fraction of the POD modes: ● and —, uncontrolled; ○ and ---- controlled

control. The reduced longitudinal integral scale (Fig. 17a) implies that the correlation of velocity streaks along the streamwise direction is adversely affected by the wall-based perturbations, implying a shortening of the streaks. Ricco [45] also observed a reduced length of the streaks with a spanwise-wall oscillation. The reduced lateral integral scale (Fig. 17b) can be ascribed to the narrower velocity streaks resulting from the generation of the regularized streamwise vortices in the near-wall region. In contrast, the lateral integral scale for the spanwise-oscillating wall is increased, which can be ascribed to the coalescence of velocity streaks during the periodic spanwise wall-movement [33].

It is of interest to examine the change of turbulent kinetic energy (TKE), especially due to the coherent structures, in the controlled TBL. The proper orthogonal decomposition (POD) provides an excellent means to extract energetic and hence large-scale coherent structures from turbulent flows [52]. In essence, the POD technique projects, following a linear procedure, a group of input data onto an orthogonal basis, which constitutes functions for the solution of an integral eigenvalue problem. The eigenfunctions are characteristic of the most

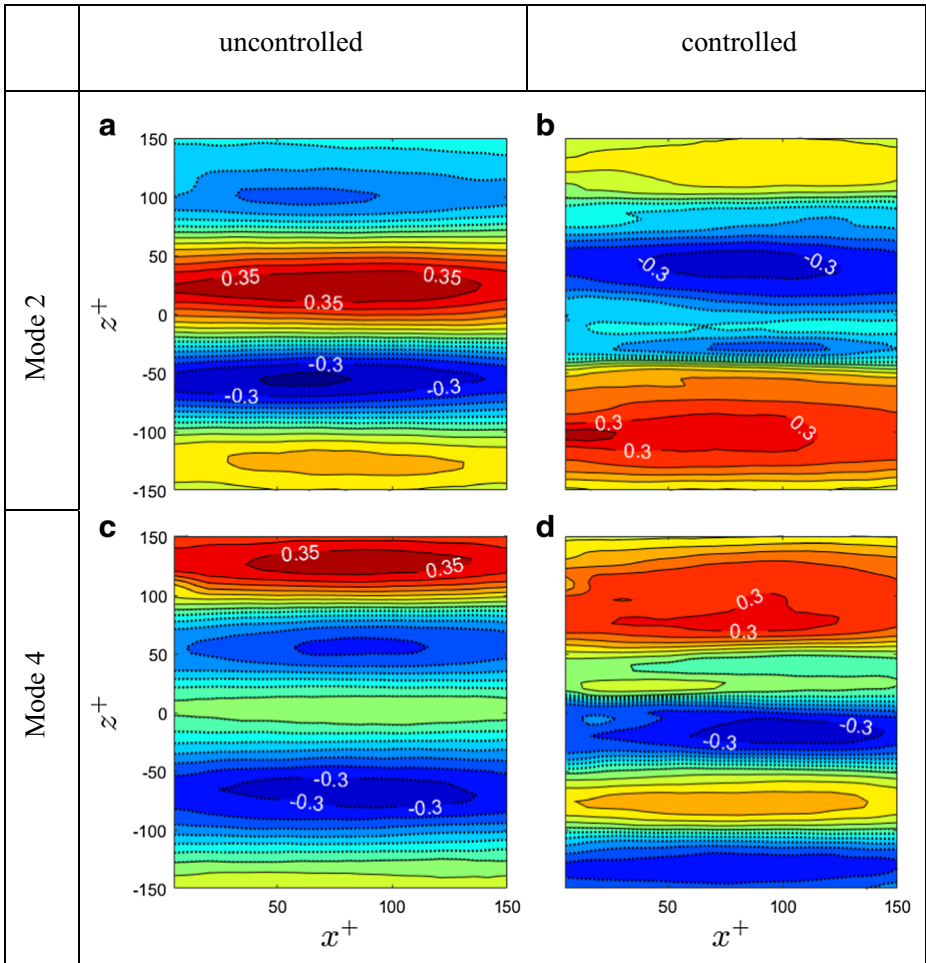


Fig. 19 The POD modes 2 and 4, in terms of iso-contours of u^+ with an increment of $\Delta = 0.05$

possible realization of the input data and are most representative of kinetic energies contained in the input data. No *a priori* assumption is required for this method, which is its greatest advantage. Please refer to Berkooz et al. [53] for more details on the POD technique. The snapshot POD [54] is presently applied for the analysis of the PIV-measured u in the xz -plane at $y^+ = 5.5$ ($x^+ \leq 160$).

Figure 18 presents the energy (i.e. eigenvalue) and cumulative energy fraction of the POD modes. The energy of modes is not normalized so that direct comparison can be made for their contributions to TKE of the turbulent structures. The lower POD modes, which are linked to the large-scale coherent structures [55], account for most of the energy. In general, the energy of the POD modes declines as the mode increases. Without control, the first two, four and ten modes contribute about 20%, 38% and 64% to the total energy, respectively. The modes beyond 100 are responsible for only about 5% of the total energy. Note that, as the mode number increases, the energy of the modes collapses very rapidly beyond the 3rd mode up to the 10th, suggesting that the lower modes play an important role in the dynamics of the near-wall turbulence. Once control is introduced, the energy of modes smaller than 10 drops appreciably, by about 8.3%, suggesting that the large-scale coherent structures are weakened. On the other hand, as highlighted by the inset in Fig. 18, the energy of modes larger than 20 is increased, echoing the increased velocity correlations or Reynolds stresses (Fig. 12). The cumulative energy is appreciably smaller with control; the departure grows until about mode 30 and then contracts for higher modes, indicating that the wall-based actuation reduces the energy associated with relatively large-scale coherent structures. Further, more POD modes are required in the controlled flow to capture a given amount of energy. For example, 17 modes are required to capture 75% of the total energy in the uncontrolled flow, while 23 modes are required in the controlled flow.

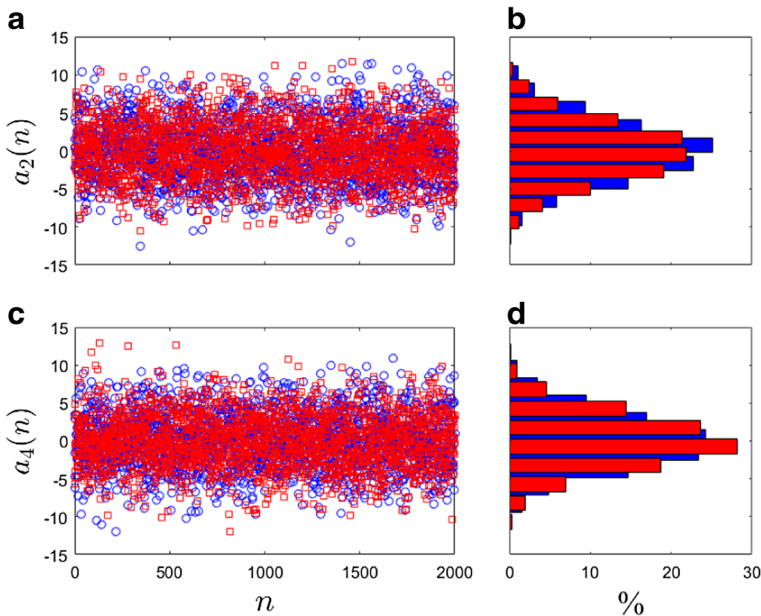


Fig. 20 Coefficients (a–b: a_2 ; c–d: a_4) of the Modes 2 and 4. Symbols in blue and red colors denote uncontrolled and controlled flows, respectively; n is the number of PIV snapshots

Several lower POD modes and their coefficients are examined in Fig. 19, in terms of the iso-contours of u^+ , and in Fig. 20, respectively, to understand the reduced TKE in the controlled near-wall flow. In the absence of control, the u^+ -contours change sign alternately along the spanwise direction and show relatively large longitudinal stretching, reflecting the typical features of high- and low-speed streaks in the near-wall region of a TBL. As the POD mode number increases, the spanwise spacing between the oppositely signed concentrations contracts, while their longitudinal extent remains almost unchanged. With control, the u^+ -contours exhibit an appreciable change in both the pattern distribution and contour level magnitude. The negative u^+ -contours become wider for mode 2; the maximum magnitudes of the positive u^+ -contours for modes 2 and 4 are reduced by about 14.3%. Furthermore, it can be seen in Fig. 20 that the coefficients of modes 2 and 4 for the controlled flow are appreciably altered, and their histogram distributions are more concentrated by comparison to the uncontrolled flow.

7 Conclusions

Various statistical analyses, including the detections of streamwise vortices and velocity streaks, spatial correlation and POD, have been performed to determine how the coherent structures are altered in a drag-reduced TBL ($Re_\theta = 1000$ or $Re_\tau = 440$), based on PIV-measured fluctuating velocities in wall-parallel and cross-stream planes in the near-wall region. Significant changes have been observed in the streamwise vortices and streaky structures when control is applied, in line with the large drag reduction that is achieved. There are three major conclusions.

There is an increase in the number and strength of the streamwise vortices but a decrease in their size in the near-wall region (Table 2). For example, the number and strength of the negative streamwise vortices are increased by 11.9% and 11.1%, respectively, while their average size and spacing are reduced by 12.2% and 21.6%, respectively. Further, the velocity correlations are altered in the near-wall region; in particular, w^+w^+ and u^+w^+ in the xz -plane at $y^+ = 5.5$ are greatly increased (Fig. 12b&c).

Velocity streaks undergo major changes. The maximum magnitude (u_{\max}) of the velocity streaks is reduced. For example, for low-speed streaks, u_{\max}^+ is about 8% lower than without control, and the averaged value is reduced by 7.5%. The spanwise gradient ($\partial u/\partial z$) of the velocity streaks is larger in the controlled flow, resulting in an increased streak strength. Further, the integral length scale along the spanwise direction is reduced under control, due to the decreased width and spacing of the velocity streaks. These observations contrast with those when control is implemented via a spanwise-wall oscillation or a spanwise oscillatory Lorentz force. In these latter cases, the low-speed streaks coalesce to form wider and weaker streaks [18].

Streaky structures are more closely spaced, smaller and more orderly than without control. In fact, the streaky structures with control exhibit a close similarity to those on a smooth wall immediately downstream of a suction strip (see Fig. 10b in [51]). It is well known that for sufficiently strong suction, relaminarization occurs and the stabilized streaks can be discerned almost until their final disappearance, that is, when the flow returns to a laminar state [56]. The flow relaminarization, at least locally, downstream of the wall-based perturbations, is fully consistent with the reduced TKE of relatively large-scale structures and the substantial drag reduction.

Acknowledgements YZ wishes to acknowledge support given to him from NSFC through grant 11632006, from RGC of HKSAR through grant PolyU 5329/11E. H.L.B. would like to acknowledge support given to him from NSFC through grant 11302062 and from State Key Laboratory of Aerodynamics through grant SKLA20130102.

Compliance with Ethical Standards

Conflict of interests The authors declare that they have no conflict of interest.

References

- Kline, S.J., Reynolds, W.C., Schraub, F.A., Runstadler, P.W.: The structure of turbulent boundary layers. *J. Fluid Mech.* **30**, 741–773 (1967)
- Robinson, S.K.: Coherent motions in the turbulent boundary layer. *Annu. Rev. Fluid Mech.* **23**, 601–39 (1991)
- Schoppa, W., Hussain, F.: Coherent structure generation in near-wall turbulence. *J. Fluid Mech.* **453**, 57–108 (2002)
- Jiménez, J.: Near-wall turbulence. *Phys. Fluids* **25**, 101302 (2013)
- Panton, R. (ed.): *Self-Sustaining Mechanisms of Wall Turbulence*. Comp. Mech. Publ, Southampton, UK (1997)
- Wallace, J.M.: Highlights of from 50 years of turbulent boundary layer research. *J. Turbul.* **13**(53), 1–70 (2013)
- Kravchenko, A.G., Choi, H., Moin, P.: On the generation of near-wall streamwise vortices to wall skin friction in turbulent boundary layers. *Phys. Fluids A* **5**, 3307–9 (1993)
- Orlandi, P., Jiménez, J.: On the generation of turbulent wall friction. *Phys. Fluids A* **6**, 634–41 (1994)
- Kim, J., Moin, P., Moser, R.: Turbulence statistics in fully developed channel flow at low Reynolds number. *J. Fluid Mech.* **177**, 133–166 (1987)
- Kim, J.: On the structure of wall-bounded turbulent flows. *Phys. Fluids* **26**(8), 2088–97 (1983)
- Kim, J.: Physics and control of wall turbulence for drag reduction. *Phil. Trans. R. Soc. A* **369**, 1396–1411 (2011)
- Jeong, J., Hussain, F., Schoppa, W., Kim, J.: Coherent structures near the wall in a turbulent channel flow. *J. Fluid Mech.* **332**, 185–214 (1997)
- Lu, S.S., Willmarth, W.W.: Measurements of the structure of the Reynolds stress in a turbulent boundary layer. *J. Fluid Mech.* **60**, 481–511 (1973)
- Smith, C.R., Walker, J.D.A.: *Turbulent Wall-Layer Vortices in Fluid Vortices*. Springer, New York (1994)
- Zhou, J., Adrian, R.J., Balachandar, S., Kendall, T.M.: Mechanisms of generating coherent packets of hairpin vortices in channel flow. *J. Fluid Mech.* **387**, 353–396 (1999)
- Hamilton, J.M., Kim, J., Waleffe, F.: Regeneration mechanisms of near-wall turbulence structures. *J. Fluid Mech.* **287**, 317–348 (1995)
- Gad-el-Hak, M.: *Flow Control: Passive, Active, and Reactive Flow Management*. Cambridge University Press (2000)
- Karniadakis, G.E., Choi, K.-S.: Mechanisms on transverse motions in turbulent wall flows. *Annu. Rev. Fluid Mech.* **35**, 45–62 (2003)
- Kim, J.: Control of turbulent boundary layers. *Phys. Fluids A* **15**, 1093–1105 (2003)
- Quadrio, M.: Drag reduction in turbulent boundary layers by in-plane wall motion. *Phil. Trans. R. Soc. A* **369**, 1428–1442 (2011)
- Bai, H.L., Zhou, Y., Zhang, W.G., Xu, S., Wang, Y., Antonia, R.A.: Active control of a turbulent boundary layer based on local surface perturbation. *J. Fluid Mech.* **750**, 316–354 (2014)
- Berger, T.W., Kim, J., Lee, C., Lim, J.: Turbulent boundary layer control utilizing the Lorentz force. *Phys. Fluids* **12**, 631–49 (2000)
- Huang, L., Fan, B., Dong, G.: Turbulent drag reduction via a transverse wave travelling along streamwise direction induced by Lorentz force. *Phys. Fluids* **22**, 015103 (2010)
- Nakanishi, R., Mamori, H., Fukagata, K.: Relaminarization of turbulent channel flow using traveling wave-like wall deformation. *Int. J. Heat Fluid Flow* **35**, 152–159 (2012)
- Tomiya, N., Fukagata, K.: Direct numerical simulation of drag reduction in a turbulent channel flow using spanwise travelling wave-like wall deformation. *Phys. Fluids* **25**, 105115 (2013)
- Koh, S.R., Meysonnat, P., Meinke, M., Schröder, W.: Drag reduction via spanwise transversal surface waves at high Reynolds numbers. *Flow Turb. Combust.* **95**, 169–190 (2015)

27. Koh, S.R., Meysonnat, P., Statnikov, V., Meinke, M., Schröder, W.: Dependence of turbulent wall-shear stress on the amplitude of spanwise transversal surface waves. *Comp. Fluids* **119**, 261–275 (2015)
28. Meysonnat, P.S., Roggenkamp, D., Li, W., Roidl, B., Schröder, W.: Experimental and numerical investigation of transversal traveling surface waves for drag reduction. *Euro. J. Mech. B/Fluids* **55**, 313–323 (2016)
29. Mamori, H., Fukagata, K.: Drag reduction effect by a wave-like wall-normal body force in a turbulent channel flow. *Phys. Fluids* **26**, 115104 (2014)
30. Kang, S., Choi, H.: Active wall motions for skin-friction drag reduction. *Phys. Fluids* **12**(12), 3301–04 (2000)
31. Choi, K.-S., DeBisschop, J.-R., Clayton, B.R.: Turbulent boundary-layer control by means of spanwise-wall oscillation. *AIAA J.* **36**(7), 1157–63 (1998)
32. Dhanak, M.R., Si, C.: On reduction of turbulent wall friction through spanwise wall oscillations. *J. Fluid Mech.* **383**, 175–195 (1999)
33. Iuso, G., Di Cicca, G.M., Onorato, M., Spazzini, P.G., Malvano, R.: Velocity streak structure modifications induced by flow manipulation. *Phys. Fluids* **15**, 2602 (2003)
34. Du, Y., Karniadakis, G.E.: Suppressing wall turbulence by means of a transverse travelling wave. *Science* **288**, 1230–34 (2000)
35. Du, Y., Symeonidis, V., Karniadakis, G.E.: Drag reduction in wall-bounded turbulence via a transverse travelling wave. *J. Fluid Mech.* **457**, 1–34 (2002)
36. Khoo, B.C., Chew, Y.T., Teo, C.J.: On near-wall hot-wire measurements. *Exps. Fluids* **29**, 448–460 (2000)
37. Huang, J.F., Zhou, Y., Zhou, T.M.: Three-dimensional wake structure measurement using a modified PIV technique. *Exps. Fluids* **40**, 884–896 (2006)
38. Sciacchitano, A., Wieneke, B.: PIV Uncertainty propagation. *Meas. Sci. Technol.* **27**, 084006 (2016)
39. Hu, J.C., Zhou, Y.: Flow structure behind two staggered circular cylinders. Part 1. Downstream evolution and classification. *J. Fluid Mech.* **607**, 51–80 (2006)
40. Sciacchitano, A., Neal, D.R., Smith, B.L., Warner, S.O., Vlachos, P.P., Wieneke, B., Scarano, F.: Collaborative framework for PIV uncertainty quantification: comparative assessment of methods. *Meas. Sci. Technol.* **26**, 074004 (2015)
41. Chong, M., Perry, A.E., Cantwell, B.J.: A general classification of three-dimensional flow fields. *Phys. Fluids A* **2**, 765 (1990)
42. Gouder, K., Potter, M., Morrison, J.F.: Turbulent friction drag reduction using electroactive polymer and electromagnetically driven surfaces. *Exp Fluids* **54**, 1441 (2013)
43. Toubert, E., Leschziner, A.: Near-wall streak modification by spanwise oscillatory wall motion and drag-reduction mechanisms. *J. Fluid Mech.* **693**, 150–200 (2012)
44. Di Cicca, G.M., Iuso, G., Spazzini, P.G., Onorato, M.: Particle image velocimetry investigation of a turbulent boundary layer manipulated by spanwise wall oscillations. *J. Fluid Mech.* **467**, 41–56 (2002)
45. Ricco, P.: Modification of near-wall turbulence due to spanwise wall oscillations. *J. Turbul.* **5**, N24 (2004)
46. Yang, L.: Turbulent Drag Reduction with Piezo-Ceramic Actuator Array. Master Degree Thesis, The Hong Kong Polytechnic University (2013)
47. Qiao, Z.X., Zhou, Y., Wu, Z.: Turbulent boundary layer under the control of different schemes. *Proc. R. Soc. A* **473**, 20170038 (2017)
48. Ricco, P., Wu, S.: On the effects of lateral wall oscillations on a turbulent boundary layer. *Exp. Therm. Fluid Sci.* **29**(1), 41–52 (2004)
49. Lardeau, S., Leschziner, M.A.: The streamwise drag-reduction response of a boundary layer subjected to a sudden imposition of transverse oscillatory wall motion. *Phys. Fluids* **25**, 075109 (2013)
50. Choi, K.-S.: Near-wall structure of turbulent boundary layer with riblets. *J. Fluid Mech.* **208**, 417–458 (1989)
51. Antonia, R.A., Fulachier, L., Krishnamoorthy, L.V., Benabid, T., Anselmet, F.: Influence of wall suction on the organized motion in a turbulent boundary layer. *J. Fluid Mech.* **190**, 217–240 (1988)
52. Lumley, J.L.: *Stochastic Tools in Turbulence*. Academic Press, London (1970)
53. Berkooz, G., Holmes, P., Lumley, J.L.: The proper orthogonal decomposition in the analysis of turbulent flows. *Annu. Rev. Fluid Mech.* **25**, 539–575 (1993)
54. Sirovich, L.: Turbulence and the dynamics of coherent structures, part I. *Quart. Appl. Math.* **45**, 561–590 (1987)
55. Fiedler, H.E., Gad-el-Hak, M., Pollard, A., Bonnet, J.-P.: Control of free turbulent shear flows. In: *Flow Control: Fundamental and Practices*, Lecture Notes. Phys. 53, pp. 336–429. Springer, Berlin (1998)
56. Antonia, R.A., Zhu, Y., Sokolov, M.: Effect of concentrated wall suction on a turbulent boundary layer. *Phys. Fluids* **7**, 2465–2474 (1995)